Materials Advances

ROYAL SOCIETY OF CHEMISTRY

PAPER

View Article Online
View Journal

Cite this: DOI: 10.1039/d6ma00421k

Indentation of glasses that produce a boundary-forming annular crack

T. M. Gross, * J. Wu, R. Yongsunthon, J. J. Price, R. E. Youngman, K. Singh, B. D. Fulmer and J. Jones

A series of boroaluminosilicate glasses are designed to span the range of Vickers indentation cracking behaviors. At one endpoint, median/radial cracking is observed, whereas the other endpoint exhibits ring and cone cracking. In the transition in cracking behavior across the glass series, a composition space is identified that produces a large boundary-forming annular crack that prevents the extension of radial cracks emanating from the indent impression. Indentation cross-sectioning shows that this unique cracking system forms as a traditional cone crack, which is then redirected back to the surface following unloading by residual stress. The percentage of volume displaced from 30 mN Berkovich scratch grooves was 10–15% for glasses that produce the annular crack. This places this new glass space on the anomalous end of the deformation continuum, but with more volume-conserving shear component than fully anomalous glass like silica. This unique combination of densification and shear enables the formation of the initial cone crack (densification contribution) and provides the residual stress (shear contribution) that causes the cone crack to be redirected back to the surface. Retardance measurements through the cross-section show that residual stresses initially associated with lateral crack extension interact with the cone crack to drive it back to the surface.

Received 26th March 2026,
Accepted 21st May 2026

DOI: 10.1039/d6ma00421k

rsc.li/materials-advances

Introduction

Indentation deformation and cracking of glasses have been studied extensively, with much of the historical work limited to commercially available soda-lime silicate and silica.[1–8] Conveniently, these glass types serve as extreme endpoints in the Vickers indentation response spectrum. Soda-lime silicate glass, categorized as a normal glass, deforms with a significant volume-conserving shear contribution.[2–5,7–10] The displaced volume results in glass pile-up in the region surrounding the indent periphery. Shear readily initiates at weak points in the glass network associated with non-bridging oxygens (NBO).[2,3] Shear faults in the subsurface act as starter cracks for larger median/radial and lateral cracking systems that appear under modest applied indentation loads.[4,5,7,8] On the other hand, silica, categorized as anomalous glass, deforms primarily by volume-reducing densification.[1,2,5,8–11] The high connectivity of the essentially NBO-free, tetrahedral network is more resistant to shear deformation.[9] Deformation by densification results in high tensile stresses at the surface during loading, thus leading to ring cracking at the indent periphery at low applied loads.[6,8,9,12] More recently, a third category of glasses was appropriately defined as intermediate, since these glasses deform with more densification than normal soda-lime glass and more shear than anomalous silica glass.[9,13] Examples explored thus far in this category are also essentially NBO-free, but the incorporation of trigonal boron into the silicate network reduces the average coordination of glass formers. This less rigidly constrained network enables greater shear when compared to silica, alleviating ring cracking stresses.[12,13] Still, the network is well connected, so densification remains high when compared to soda-lime silicate and the resulting sub-surface damage is minimal.[9,13] Trigonal boron enables both shear and densification, shear from the less constrained network and densification from the transition from trigonal to tetrahedral coordination under pressure.[14,15] In a subset of intermediate glasses with high trigonal boron content, high indentation crack resistance is achieved through delocalized shear deformation that enables displacement without shear faulting.[9]

Berkovich nanoscratch experiments have recently been used to characterize the amount of shear displacement in various glass types, thus providing a straight-forward means of defining glasses as normal, anomalous, or intermediate.[9] While the Vickers tip is commonly used in large impression micro-indentation testing, the Berkovich tip is used in nano-scratch experiments where the tip of the indenter has a considerable influence on the deformation. The precision radius at the apex of the three-sided Berkovich tip is preferred over the variable junction-offset present in four-sided Vickers tips for

Science and Technology, Corning Research and Development Corporation, Painted Post, New York 14870, USA. E-mail: grosstm@corning.com

nano-indentation and nano-scratch studies. Since the Berkovich and Vickers tips provide the same contact area to indentation depth ratio, they may be used interchangeably, with preference depending on the loading regime. The volume displaced by shear into the pile-up regions for a 30 mN Berkovich scratch is approximately 30% for intermediate glasses, whereas normal soda-lime silicate and anomalous silica have displaced volumes of 50% and 9%, respectively.[9]

The establishment of intermediate glasses demonstrates that the indentation response of glasses is a continuum between the well-known end-point glasses, which are defined as normal and anomalous. It is also not satisfactory to simply place all glasses in one of these three buckets. Along the transition in indentation response behavior, we encounter glasses that have their own unique characteristics. The present study highlights a borosilicate composition window near the anomalous end of the spectrum that forms a unique annular crack with a diameter several times larger than the indentation major diagonal length.[16,17] Due to its ability to act as a boundary against the extension of strength-limiting radial cracks, it is referred to as a "boundary-forming annular crack" in the present work.

Experimental

Glass sample preparation

A series of sodium boroaluminosilicate glasses were prepared from sand (Puresil 100C-1; Sibelco Bao Lin Co., Ltd), calcined alumina (A-2 unground; Almatis, Inc.), boric acid (technical grade; Chemical Distributors Inc.), and sodium carbonate (soda ash grade 260; Amrex Chemical Co., Inc.). For each glass composition, 2 kilograms (kg) of the batch was mixed in a Turbula mixer for 15 minutes, then melted at 1650 °C for 12 h in a covered platinum crucible. The molten glasses were poured onto a clean, stainless-steel table and transferred to annealing furnaces set to 600 °C. Glasses were annealed for 8 h and cooled in the furnace at a rate of 100 °C h^{-1}. The compositions were analyzed by X-ray fluorescence (XRF) and B_2O_3 content was determined by inductively coupled plasma–optical emission spectroscopy (ICP-OES). Samples for mechanical testing were prepared into testing coupons with dimensions of 50 × 50 × 1 mm. The surfaces of the samples were ground using 150 and 320 grit resin bonded diamond in water. The surface was then polished to an optical finish using 22 μm Al_2O_3 in water, followed by a cerium oxide and water slurry. Specimens of commercially available, fusion-drawn Corning® Fusion5® at 1 mm thickness were also used for mechanical testing. Samples were prepared as 50 × 50 mm coupons by a scribe and break process.

To demonstrate the role of fictive temperature in boundary-forming annular crack formation, select specimens were heat-treated to set the fictive temperatures equal to the strain pt, anneal pt, and 10^{10} Pa s temperatures. To ensure full relaxation to the specified fictive temperature, specimens were heat-treated at times significantly longer than the estimated minimum structural relaxation time of 30τ, where the relaxation time, τ, is equal to ν/G. The ν is the viscosity at the specified fictive temperature target, *i.e.*, $10^{13.68}$ Pa s for the strain pt and $10^{12.18}$ Pa s for the annealing point. The value for shear modulus, G, is taken from the resonant ultrasound spectroscopy (RUS) data at room temperature and in the as-annealed state. The lower G values at the fictive temperatures of interest further justify the additional heat-treatment times well beyond 30τ. Heat treatment at the strain point was performed for a duration of one week, heat treatment at the annealing point was performed for 4 hours, and heat treatment at 10^{10} Pa s was performed for 10 minutes. A gentle fan cooling was appropriate to lock in the fictive temperatures for samples heat treated at the strain and annealing points due to their lengthy relaxation times. For the sample heat treated at 10^{10} Pa s, the specimen was quickly removed from the furnace and placed into an air quenching apparatus consisting of three high velocity fans to lock in the fictive temperature as close to the target as possible.

Physical property measurement

Physical property measurements were performed on the prepared glass compositions including density measurement by the buoyancy method,[18] coefficient of thermal expansion (CTE) measurements from 25–300 °C by dilatometry,[19] strain and annealing point determination by beam bending viscosity (BBV),[20] softening point measurement by parallel plate viscosity (PPV),[21] and measurement of elastic properties *via* resonant ultrasound spectroscopy (RUS).[22] Refractive index at 589.6 nm was measured using an Abbe refractometer.[23] The 10^{10} Pa s temperature was estimated for each of the crucible melted glasses by fitting a Fulcher curve through the strain, annealing, and softening points. The 10^{10} Pa s temperature is representative of the fictive temperature of fusion-formed glass.[24]

Structural characterization

^{11}B MAS NMR experiments were conducted with a commercial spectrometer (Agilent DD2) and a 16.4 T narrow-bore superconducting magnet. The resonance frequency of ^{11}B at this magnetic field was 224.52 MHz. Samples were powdered using an agate mortar and pestle and packed into 3.2 mm outer diameter zirconia rotors, with sample spinning controlled to 20 ± 0.001 kHz. 200–1000 scans were co-added for each sample, making use of 0.6 μs radio-frequency pulse widths (π/12 tip angle) and a recycle delay of 10 s between scans. Data were processed using commercial software and without any apodization. The ^{11}B MAS NMR spectra were frequency referenced using a secondary shift reference (aqueous boric acid) at 19.6 ppm relative to the standard boron trifluoride etherate $BF_3O(Et)_2$ reference. Spectra were deconvoluted using DMFit,[25,26] with the "Q mas $\frac{1}{2}$" model representing the 2nd-order quadrupolar broadened lineshapes of the trigonal boron resonances, and the "Gaus/Lor" model approximating the tetrahedral boron lineshapes. N_4 (the ratio of four-coordinated to total boron) was determined by integrating the areas of these peaks, and with consideration of spinning sidebands and a strongly overlapping contribution from the satellite transitions of the four-coordinated boron.[27]

Mechanical testing

Vickers indentation was performed at 25 °C and 50% relative humidity using a LECO LV800AT macrohardness tester with a dwell time fixed at 10 s. Loading and unloading rates were displacement controlled at 60 μm s^{-1}. Optical imaging of the surface view of indents was performed 5 minutes after indentation. An indentation cross-section of a Fusion5® specimen exhibiting the boundary forming annular crack was prepared using the technique developed by Hagan.[6,7] The LECO LV800AT Vickers hardness tester was used to make the indents at the tip of a pre-crack. The pre-crack is created by initially making an indent at 10 kilograms force (kgf). The 10 kgf load is high enough to produce radial cracks that can be propagated by bending the glass specimen by hand. Manual bending is used to extend the pre-crack by at least 10 major diagonal lengths of the 10 kgf indent. One major diagonal of the indent impression was aligned with the pre-crack, so when fracturing the sample, the indents would be bisected into two halves for analysis. Indent surface and cross-section images were captured using a Nikon Eclipse ME600 compound optical microscope with polarized light.

To demonstrate the boundary-forming capability of the annular crack, a 1 mm thick Fusion5® specimen was indented at 2 kgf, and then placed on a hot plate at 130 °C. After 5 minutes, ice water was dropped onto the indent location. Images of the radial cracks before and after thermal shock were captured with a compound optical microscope.

Scratches were made in the $Na_2O{\cdot}Al_2O_3{\cdot}B_2O_3{\cdot}SiO_2$ (NABS) and Fusion5® glasses with a Berkovich tip at a constant load of 30 mN using an MTS Nano G200 nanoindenter. A lateral edge of the indenter was pointed forward when making scratches. The 30 mN load was selected since higher loads produced significant machine curling of the pile-up material, thus making subsequent pile-up measurements difficult. The scratch impression area and pile-up areas were measured using atomic force microscopy (AFM). The AFM scans were performed on a Bruker Bioscope Catalyst in tapping mode using TESP probes. The substrates were manually positioned such that the scratches were perpendicular to the fast scan (horizontal) axis, to ensure that any tip geometric convolution effects would be consistent across all samples. Slow scan rates, low feedback gains, and moderate tapping setpoints were used to minimize "overshoot" artifacts at the pileup regions and optimize topographic accuracy. The scratches were centered relative to the scan region and the scans were flattened with a second order polynomial fit to flat (control) regions on both sides of the scratches. MATLAB was used to calculate the scratch and pileup areas for every scan line (row) of the 512 × 512 pixel height images. The averages were calculated from values extracted across all rows in an image, only excluding anomalous scan lines. The uncertainties quoted for all extracted parameters represent true variability of the calculated areas, not instrumental error. The variability of the area calculations is mostly due to real variability of the scratch topography; however, some of it can be attributed to polishing flaws on the substrate surfaces. Since the pile-up is consistent along the scratch track, we may interchangeably refer to displaced material as % displaced area or % displaced volume.

Retardance measurement

An experimental setup was prepared to measure the evolution of the stress field during the formation of annular ring cracks. The *in situ* photoelastic measurement apparatus was built around the LV800AT LECO Vickers Hardness Tester. Retardation measurements were taken through cross-sections of indents made at 3 kgf with a 10 s dwell time. Measurements were taken immediately after unloading, then again at 750 ms, 8 s, and 12 s. An illumination module was constructed with a Thorlabs M530L4 530 nm LED, diffuser (D), linear polarizer (LP), quarter-wave plate (QWP) and 25.4 mm focal length collimation lens (CL) producing uniform collimated right-circularly polarized illumination through an optically polished 10 mm × 5 mm × 3 mm Fusion5® specimen. Spatially resolved Stokes intensity measurements were captured using an imaging module comprised of a telecentric relay system. This relay system imaged the plane of the indent onto the focus of a Newport M-20X objective lens (OL) which was used to magnify the image onto the sensor of a LUCID Vision Labs PHX050S1-PC Polarization camera (PC) operating at ~20 fps. The camera sensor simultaneously captures all four required intensity projections and images are post-processed to extract the integrated retardance and slow-axis angles from the measurement of the S_1 and S_2 Stokes parameters of the output light.[28] A schematic of the experimental system is shown in Fig. 1.

Results

The batched and analyzed compositions for the NABS crucible melted glasses are given in Table 1. The series is designed such that B_2O_3 is increased at the expense of Na_2O when going from NABS-1 to NABS-4. A brief description of the structural role of Na^+ is important to understand the transition from NABS-1 to NABS-4. In general, Na^+ is first consumed during charge balancing Al^{3+} and thus allows it to substitute into Si^{4+} positions in the tetrahedral network of the glass. Once Al^{3+} ions that are present are charge compensated, Na^+ will next charge compensate B^{3+} such that it can also substitute for Si^{4+} at tetrahedral positions.[29] The remaining Na^+ in excess of both Al^{3+} and B^{3+} modifies the glass network by creating non-bridging oxygens.

As shown in the ^{11}B NMR spectrum in Fig. 2a, the percentage of boron in tetrahedral coordination is 91.2% for NABS-1.

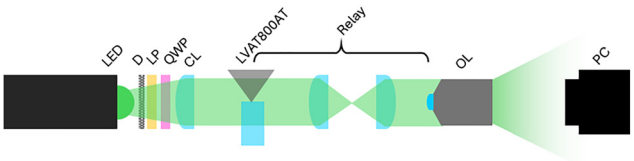

Fig. 1 Schematic of the *in situ* photoelastic measurement system affixed to a LVAT800AT Vickers hardness tester.

Table 1 Compositions and physical properties of lab melted glasses

Glass Code	NABS-1	NABS-2	NABS-3	NABS-4
Batched composition (mol%)				
SiO_2	74	74	74	74
Al_2O_3	2	2	2	2
B_2O_3	6	11	16	21
Na_2O	18	13	8	3
Analyzed composition (mol%)				
SiO_2	77.18	78.97	76.42	75.54
Al_2O_3	1.98	2.04	2.04	2.01
B_2O_3	4.66	8.67	14.71	19.76
Na_2O	16.14	10.28	6.8	2.66
Minor constituents	0.04	0.04	0.03	0.03
Na_2O–(Al_2O_3 + B_2O_3)	9.50	−0.43	−9.95	−19.11
Physical Properties				
Density (g cm^{-3})	2.428	2.397	2.270	2.147
Coefficient of thermal expansion × 10^{-6} ($°C^{-1}$)	7.99	6.03	4.48	3.52
Strain Pt. (°C)	503	556	501	436
Anneal Pt. (°C)	542	596	546	491
Softening Pt. (°C)	720	770	755	781
10^{10} Pa s Temperature (°C)	605	659	620	586
Poisson's ratio	0.200	0.186	0.195	0.217
Young's modulus (GPa)	70.40	75.98	64.67	48.33
Shear modulus (GPa)	29.3	32.06	27.10	19.86

Since NBAS-1 contains 9.5 mol% Na_2O in excess of the combined amount of Al_2O_3 and B_2O_3, the glass has considerable number of non-bridging oxygens (NBOs), making this glass the most "normal" in the NABS series. Non-bridging oxygens reduce connectivity and break the ring structures, such that the network may be thought of as partially collapsed. The highest density value (2.428 g cm^{-3}) of the series results from this NBO-rich, collapsed network containing a high concentration of space filling Na^+ ions.

Moving across the series to NABS-2, B_2O_3 is increased at the expense of Na_2O to make Na_2O nearly equal to (Al_2O_3 + B_2O_3). This charge balanced composition without excess Na^+ has limited NBOs and a high concentration of tetrahedral boron, as shown in Fig. 2a (N_4 = 74.7%). This glass has the lowest Poisson's ratio in the series, thus indicating the highest degree of covalency, *i.e.* a high degree of tetrahedral coordination with few NBOs. This high degree of network connectivity leads to the highest values for strain and annealing points as well as the highest values for elastic moduli.

Next, the NABS-3 composition has an (Al_2O_3 + B_2O_3) content than exceeds Na_2O by 9.95 mol%, therefore, the glass is free of NBOs and because there is insufficient Na^+ to charge compensate B^{3+}, the glass contains a considerable fraction of trigonal boron. As shown in Fig. 2a, N_3 is 66.9% while N_4 decreases to 33.1%.

The final glass in the series, NBAS-4, contains Na_2O in slight excess of Al_2O_3, so the glass is NBO-free and essentially all of the boron is present as N_3 as shown in Fig. 2a. With very little Na_2O content, the glass is made up of almost all glass-forming oxides. With few space filling modifier ions, the glass has the lowest density and is considered the most anomalous of the glasses in the series.

Table 2 tabulates the properties of commercially available Corning® Fusion5® glass. This glass is a version of NABS-3 that was modified to optimize manufacturability and to tune in the attributes required for a windshield glass application. Structurally, this glass may be considered a close cousin to NABS-3. The Fusion5® composition is proprietary and includes other modifier ions besides Na^+. In Table 2, the term R_xO is defined as the sum of alkali and alkaline earth oxides. A comparison of the properties shown in Tables 1 and 2 for NABS-3 and Fusion5, respectively, reveals similar properties with the notable exception of the softening point. This property was

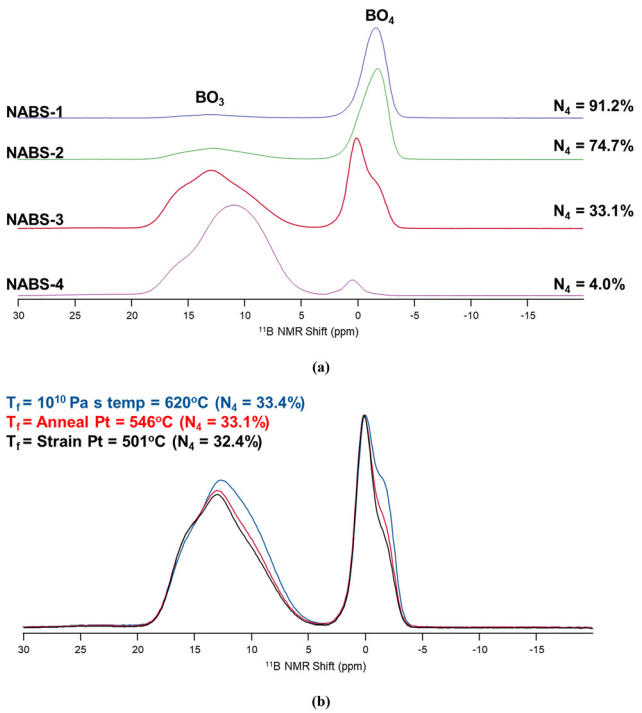

Fig. 2 (a) ^{11}B NMR on the NABS glass series with fictive temperatures set to the respective annealing point. Temperatures (b) ^{11}B NMR on NABS-3 at various fictive temperatures.

Table 2 Physical properties of Fusion5®

Glass ID	Fusion5®
R_xO–(Al_2O_3 + B_2O_3)	−8
Density (g cm^{-3})	2.266
Coefficient of thermal expansion × 10^{-6} ($°C^{-1}$)	4.66
Strain Pt. (°C)	496
Anneal Pt. (°C)	542
Softening Pt. (°C)	777
Poisson's ratio	0.190
Young's modulus (GPa)	63.70
Shear modulus (GPa)	26.50

specifically tailored to obtain the desired sagging temperature for Fusion5® in the windshield forming operation.

The ^{11}B NMR spectra in Fig. 2a also show that the BO_4 peak shifts to the left when going across the series from NABS-1 to NABS-4. The peak centered at approximately −2 ppm is representative of B surrounded by four Si ions.[30] The peak centered at approximately 0 ppm represents B surrounded by 2 to 3 Si ions and 1 to 2 B ions.[30] This interpretation is consistent with the concentration of B increasing substantially across the series.

Vickers indents are shown in Fig. 3 for glasses in the NABS series at 1 and 2 kgf. Each glass was heat-treated to set the fictive temperature to the respective annealing point temperature prior to indentation. Median/radial cracking is observed for NABS-1 and NABS-2. On the other hand, the ring and cone cracking response for NABS-4 is characteristic of anomalous glass. In between these two types of indentation cracking responses, a unique response is observed for NABS-3. At 1 kgf, a semicircular crack is observed on the bottom half of the indent that is just outside of the radial cracks. At 2 kgf, this circular crack again forms and completely surrounds the indent impression and radial cracks. Since this circular crack blocks the extension of radial cracks, it is referred to as a "boundary forming annular crack". Boundary forming annular crack formation occurs after the full unloading cycle, so it is driven by residual stress. The magnitude of residual stress depends on the amount of deformed volume, so it is then expected that a residual stress-driven cracking system will be more developed at higher indentation loads. Since the annular crack was partially formed for NABS-3 at 1 kgf as shown in Fig. 3c, the effect of minor structural changes on cracking behavior was examined by changing the fictive temperature. As shown in Fig. 4, the more compact structure with a lower fictive temperature, *i.e.*, T_f = strain pt. = 501 °C, moves towards normal cracking behavior, whereas the more open structure with a higher fictive temperature, *i.e.*, T_f = 10^{10} Pa s = 620 °C, moves towards anomalous behavior and more pronounced annular cracking. The impact of fictive temperature on refractive index and density is shown in Fig. 5 for NABS-3. The thin 1.0 mm refractive index parts were suitable for setting the fictive temperature above the anneal pt. since they could be rapidly cooled without thermal shock cracking. Challenges with rapid cooling of the thick density samples prevented proper resetting of the

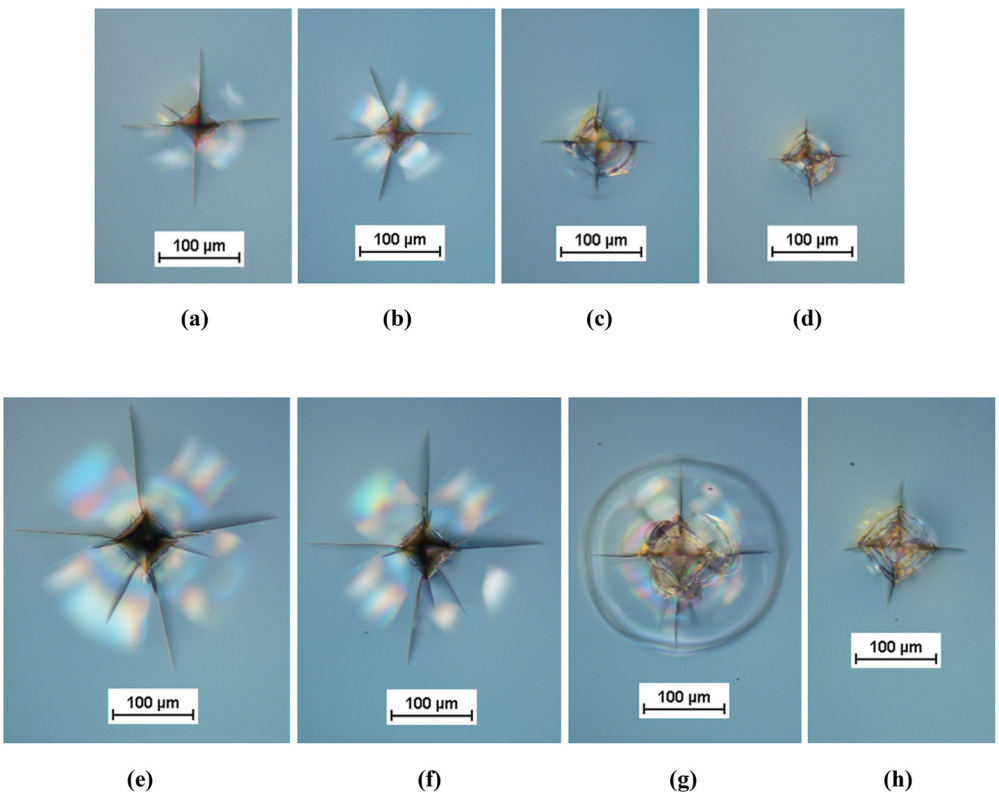

Fig. 3 Vickers indents at 1 kgf in (a) NABS-1, (b) NABS-2, (c) NABS-3, and (d) NABS-4. Vickers indents at 2 kgf in (e) NABS-1, (f) NABS-2, (g) NABS-3, and (h) NABS-4. Glasses were heat-treated to set the fictive temperatures equal to the respective annealing point temperatures prior to indentation.

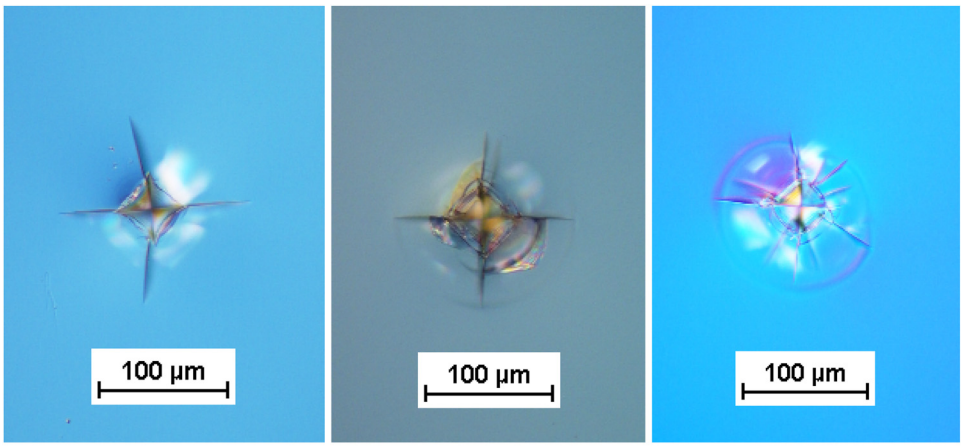

Fig. 4 Vickers indents at 1 kgf in NABS-3 at (a) fictive temperature = strain pt temperature, (b) fictive temperature = annealing point temperature, (c) fictive temperature = temperature at 10^{10} Pa s viscosity.

fictive temperature above the anneal pt. Therefore, the refractive index was measured at all three fictive temperatures, while density was only measured at the anneal and strain points, where relaxation times are considerably longer and slower cooling is adequate. As shown in Fig. 5, the refractive index and density both decrease with increasing fictive temperature as expected. The linear change in index in this fictive temperature range gives confidence that the density change will also remain linear and the density at T_f = 620 °C is estimated to be 2.267 g cm^{-3} by the linear equation provided on the plot. The molar volume for glass at each fictive temperature is calculated by dividing the molecular weight by the density. The molar volumes for NBAS-3 at fictive temperatures of 501, 546, and 620 °C are 27.49, 27.51, and 27.55 cm^3 mol^{-1}, respectively. The impact of fictive temperature on boron coordination is shown in Fig. 2b for NABS-3. A slight increase in N_4 is observed as fictive temperature is increased, with the shoulder at ∼−2 ppm becoming more pronounced at higher fictive temperatures.

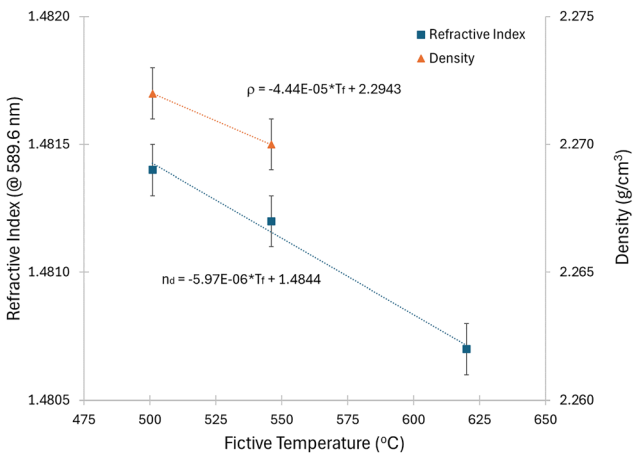

Fig. 5 Refractive index and density *vs.* fictive temperature for NABS-3.

The initiation mechanism of the boundary forming annular crack was examined by cross-sectioning through the major diagonal of a 3 kgf Vickers indent in Fusion5® as shown in Fig. 6b. The surface view of an indent in Fusion5 at 2 kgf is shown in Fig. 6a and resembles the appearance of NBAS-3 in Fig. 3g. The cross-sectioned view shows that this glass forms a cone crack characteristic of anomalous glass such as silica on the loading half-cycle. Unexpectedly, the cone crack makes a ∼90° turn following unloading and is redirected back towards the surface to form the annular ring. Since cross-sectioning required many specimens/attempts to dissect the indent impression and capture the crack turning event, production-grade Fusion5® glass was utilized. In typical indents performed at 2 kgf the boundary forming annular crack intersects the surface every time, however, when conducting the cross-sectioning technique the redirected crack does not make it all the way to the surface. Furthermore, we only see redirection on one side, which happens to be the side opposite the starter crack. Indenting at the tip of the starter crack, *i.e.*, on a glass-to-glass interface, has a clear influence on the residual stress field as reported elsewhere.[31]

Fig. 7 shows the result captured by the *in situ* retardance measurement system after unloading from a 3 kgf peak load

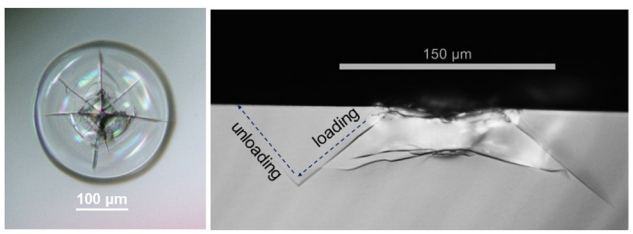

Fig. 6 (a) Surface view of 2 kgf Vickers indent in Corning® Fusion5® with a boundary forming annular crack. (b) Cross-sectional view of 3 kgf Vickers indent showing the cone crack that forms on the loading half cycle and the redirection of the cone crack to the surface on the unloading cycle.

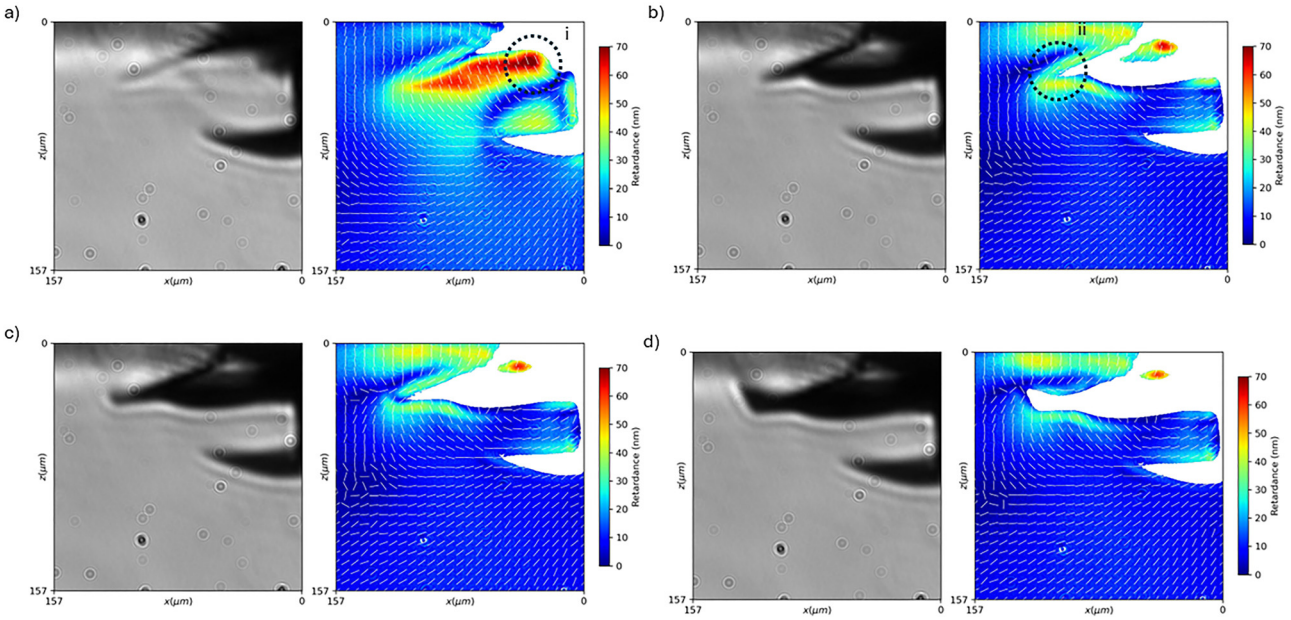

Fig. 7 Intensity (left panel) and retardance (right panel) images of crack systems formed after a 3 kgf Vickers indent on Fusion5 glass (subsampled slow-axis lines are overlayed on the retardance image). Images shown were taken (a) immediately after unloading, (b) 750 ms after unloading, (c) 8 s after unloading and (d) 12 s after unloading. Regions of interest showing retardance concentrations before extension of (i) lateral and (ii) ring cracks.

Vickers indent in Fusion5® glass. Immediately after the indentation, a notable stress concentration could be observed close to the plastic zone from which a lateral crack rapidly extended after ~750 ms, the direction of crack growth coincided with the normal of the slow-axis (*i.e.*, principal tensile stress axis), there was also notable residual stress around the cone crack which initiated during loading with tensile axes along the direction of the cone. The tip of the lateral crack settled into a position near the stress concentration at the tip of the cone crack, after ~8 s, stress appeared to be relieved at the coinciding crack tips, where the crack front was redirected normal to the residual tensile stress axis of the cone crack (*i.e.*, back towards the surface). The redirected crack slowly extended toward the surface over ~4 s after its initiation.

Fig. 8 shows images of a 2 kgf Vickers indent in Fusion5®, both before and after thermal shock. Several of the radial cracks extend following thermal shock, but are shown to terminate at the boundary-forming annular crack. When the same indent & thermal shock test is conducted on soda-lime silicate in the same 50 mm × 50 mm × 1 mm part geometry, radial cracks extend from the indent to the edges of the specimen.[16]

To categorize the glasses along the deformation continuum between normal and anomalous glass, 30 mN Berkovich scratch pileup measurements were performed. As shown in previously published work on Berkovich scratch deformation, the amount of material displaced by volume-conserving shear can be quantified using AFM measurements.[9,32] Fig. 9 shows the AFM linescans for (a) anomalous silica glass, (b) intermediate CABS25, and (c) normal soda-lime silicate.[32] The percentages of the impression volumes displaced into the pileup regions were 9%, 32%, and 50%, respectively. When we conduct the same analysis on the NABS series and Fusion5® glass, the space in between anomalous glass and our previously defined intermediate

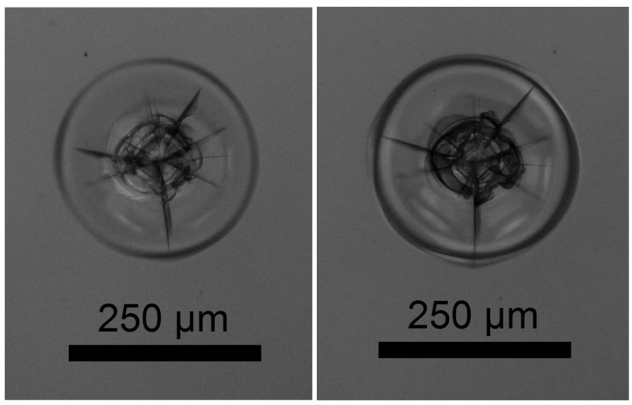

Fig. 8 (a) Image of indent in Fusion5® after 2 kgf indent. (b) Image of the same indent after heating to 130 °C and thermal shocking with ice water.

glass is interrogated. The NABS-1, NABS-2, and NABS-3 glasses had displaced volumes of 26 ± 3%, 19 ± 1%, and 10 ± 3%, respectively. An overlap of a characteristic linescan for each NABS glass is shown in Fig. 10. The cleaning procedure used to ensure high resolution AFM measurements resulted in pitting in NABS-4, so the pile-up measurement is not included. Fusion5® glass was also measured and had a displaced volume of 15 ± 1% as shown in Fig. 11. A visual representation of where the NABS glasses and Fusion5® reside on the deformation continuum is provided in Fig. 12. NABS-3 and Fusion5® are labeled (BF) in the figure for their ability to form boundary forming annular cracks by Vickers indentation in specimens with the fictive temperature set to the annealing point temperature. These glasses are near the anomalous end of the spectrum, but with slightly more volume

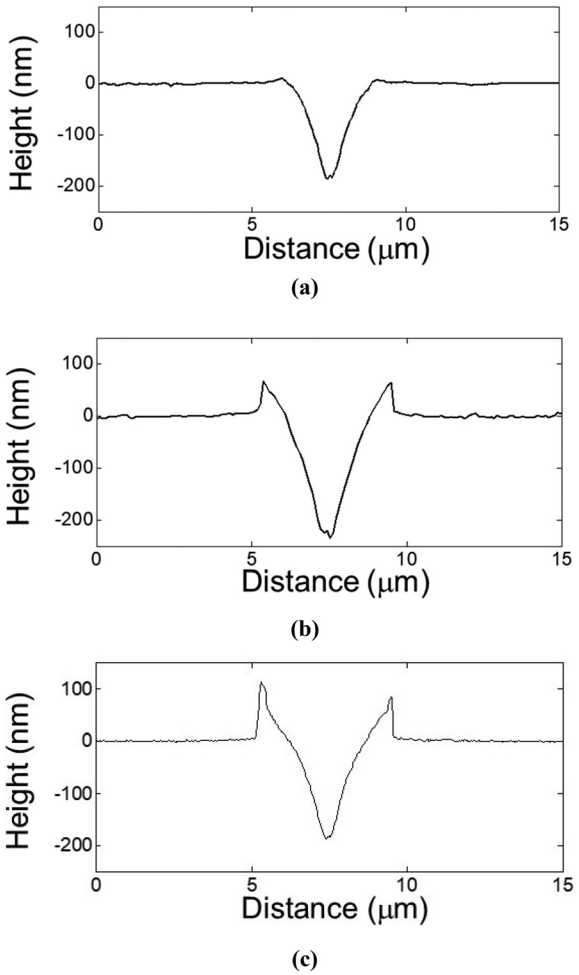

Fig. 9 AFM scans across 30 mN Berkovich scratches in (a) anomalous silica glass, (b) intermediate CABS25 glass, and (c) normal soda-lime silicate glass. The percentage of material displaced into the pileup region is 9%, 32%, and 50% for these examples of anomalous, intermediate, and normal glass, respectively. Figure reproduced from Gross[9] following STM permissions guidelines.

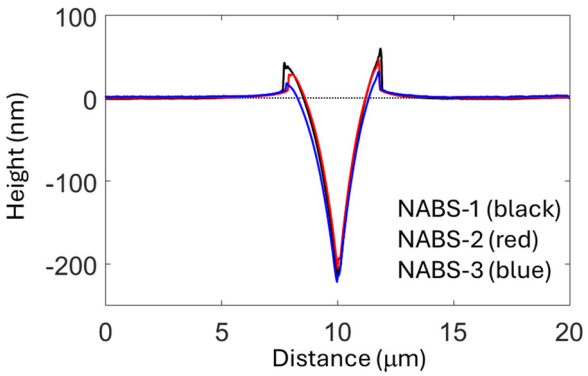

Fig. 10 AFM line scan across a 30 mN Berkovich scratch in NABS series glasses. The percentage of material displaced into the pile-up regions is 26%, 19%, and 10% for NABS-1, NABS-2, and NABS-3, respectively.

conserving shear deformation than silica. NABS-1 and NABS-2 are labeled (I) as additions to the previously defined intermediate

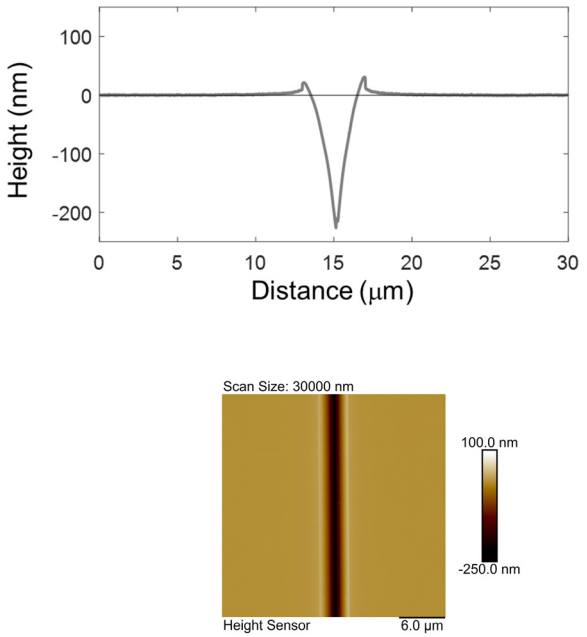

Fig. 11 (a) AFM scan across a 30 mN Berkovich scratch in Fusion5® glass. The percentage of material displaced into the pile-up region is 15%. (b) AFM image of Berkovich scratch.

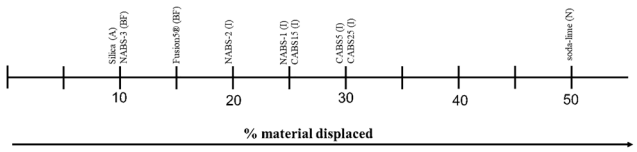

Fig. 12 Schematic representation of the indentation deformation continuum. Glasses are classified according to indentation deformation and cracking behavior by the amount of displaced material from the Berkovich nanoscratch. Classifications are as follows: (N) normal, (I) intermediate, (A) anomalous, and (BF) boundary forming.

space.[9] Like the intermediate CABS glasses described previously, they have significantly greater shear than anomalous silica and significantly greater densification than normal soda-lime silicate.[9] As with other intermediate glasses, NABS-1 and NABS-2 are advantageous for median/radial crack resistance and deform with enough shear to prevent ring and cone cracking.[9] The intermediate NABS-1 and NABS-2 have a median/radial cracking threshold of 0.5–1.0 kgf. The pile-up volumes were also measured for NABS-3 at the three fictive temperatures studied. The results were $10.8 \pm 0.6\%$, $9.7 \pm 2.7\%$, and $9.5 \pm 1.3\%$, for fictive temperatures of 501, 546, and 620 °C, respectively.

Discussion

In this study, a series of glasses were designed to show the transition in indentation behavior from glass that deforms with an intermediate amount of shear (median/radial crack forming) to highly densifiable, anomalous glass (ring/cone crack forming). The series passes through a composition,

NBAS-3, that demonstrates boundary forming annular cracking. The images in Fig. 3, particularly in images e–h, show this transition clearly. The relative contributions to deformation from densification and shear allow us to better characterize these glasses and understand our observations. In previous work, the amount of volume displaced *via* shear into the pileup region for 30 mN Berkovich scratches was measured by AFM line scans for various glass types as shown in Fig. 9. The three glass categories, *i.e.*, normal, intermediate, and anomalous, provide points of reference on the scale of the deformation continuum shown in Fig. 12. The region between the previously defined intermediate glasses (26–32% displaced volume) and anomalous glasses (9% displaced volume) was targeted when designing the NABS glass series to seek the location of glasses that display the boundary forming annular crack. The displaced volume measurements of NABS-1, NABS-2, and NABS-3 are given in Fig. 10 and cover the desired range with values of 26, 19, and 10%, respectively. As shown in Fig. 11, the Fusion5® production glass has a displaced volume of 15%, also falling within our target range of exploration. When looking again at the deformation continuum scale in Fig. 12, it is shown that the boundary forming crack appears at displaced volumes of 10 and 15% for NABS-3 and Fusion5® glasses, respectively. The location near the anomalous end of the scale is critical so that the surface tensile stress surrounding the indenter during loading is high enough that a ring crack forms at the periphery of the indent and extends into the subsurface to make a classic cone crack.[12] This is shown as the crack that formed during the loading cycle in Fig. 6b. Following unloading, the unexpected redirection of the crack towards the surface to create the boundary forming annular crack is observed. The formation of the large annular crack often takes several minutes to form following unloading, as the residual stress drives this crack back towards the surface. It is typical that a semi-circle will form first, followed by the formation of the complete annular crack as the semi-circle extends on a path around the indent. In typical anomalous glasses like silica, this crack redirection is not observed. We also do not see it in the most anomalous glass of our series, NABS-4. The residual stress that drives the boundary forming crack back to the surface is unique to glasses like NABS-3 and Fusion5® that have greater shear than typical anomalous glasses as shown in Fig. 12. While NABS-3 has only slightly higher overall displaced volume than silica, the visual comparison from Fig. 9a and 10 shows noticeable pile-up for NABS-3 that is not present for silica. The 3% error bars for the measurements for both NABS-3 and silica may lead to the unexpectedly similar % displaced volume. With replicate measurements at various fictive temperatures for NABS-3 all providing values near 10%, the emphasis of future work will be to reduce the error on measurements made on silica. The value of the $15 \pm 1\%$ displaced volume for the near perfect surface on the fusion produced Fusion5® can be taken with higher confidence to define a position on the continuum that produces a boundary-forming annular crack. The positions of the NAB-3 and Fusion5® glasses on the deformation continuum suggest a unique combination of deformation by shear and densification modes. Cone crack redirection back to the surface may be explained by considering the residual stress contribution from the greater shear contribution for these glasses.[12] In glasses that deform with more shear, the residual stress field that drives lateral cracks is significantly higher than that in anomalous glasses.[12,13] Typically, lateral cracks originate at the bottom of the deformation zone boundary and initially propagate outward in the direction parallel to the glass surface after unloading. At some distance away from the indent, the lateral cracks can turn upward to intersect the surface and create chips.[8] As shown in Fig. 6b, traditional lateral cracks form in Fusion5® in the typical location at the bottom of the deformation zone and extend outward until they meet the cone crack boundary. While the lateral cracking system terminates at the cone crack boundary, the residual stress field is still present. Fig. 7 shows a time series of retardance measurements taken through the cross-section of Fusion5®. The lateral crack again terminates on this side of the cone crack, but the lateral crack-driving residual stress field moves towards the tip of the cone crack, then wraps around it in a manner that drives it back to the surface. In previous work by Tandon *et al.*, a cracking system that appears to be a boundary-forming annular crack was shown.[33] This cracking system was described as an interaction between a lateral crack and a cone crack, similar to the current work. Since the NABS-1 and NABS-2 have characteristics of intermediate glass, they are labeled as such in Fig. 12 and provide an expansion to this previously defined space.

The region of the deformation continuum that produces the boundary forming annular crack is now defined in Fig. 12, but the formation of this crack is dependent on the indentation load. At 2 and 3 kgf, the annular crack readily forms, but at 1 kgf, it only partially forms, as shown for NABS-3 in Fig. 3c. The partially formed crack provides the opportunity to study the impact of fictive temperature on cracking. For the sample treated to set the fictive temperature to the strain pt, the molar volume is the lowest at 27.49 cm^3 mol^{-1} indicating the highest packed structure of the three fictive temperatures studied. In turn, the displaced volume is also the highest at 10.8%. Surprisingly, this slight move along the scale towards normal glass results in the suppression of the initial ring crack and normal median/radial cracking is observed. By setting the fictive temperature to the annealing point (the standard condition for our study), the molar volume increases to 27.51 cm^3 mol^{-1} and the displaced volume is reduced slightly to 9.7%. As previously mentioned, this condition shows a partially developed annular crack. At the highest fictive temperature of 620 °C, the molar volume is the highest at 27.55 cm^3 mol^{-1}, the displaced volume is reduced again to 9.5%, and a fully developed annular crack is observed. High fictive temperature and the associated open network are more prone to densification, thus increasing the ring crack forming stresses at the periphery of the indent and the stresses that drive formation of the initial cone crack. A well-developed cone crack is a necessary pre-requisite for the formation of the boundary forming annular crack, as shown in Fig. 6b. At low indentation loads, *e.g.* 1 kgf, this is more challenging and apparently requires the boost provided by a more open, more anomalous,

and thus more densifiable structure. Another interesting finding from the fictive temperature study is that lower fictive temperatures show more B–O–B bonds and higher fictive temperatures show more B–O–Si bonds among the tetrahedrally coordinated boron (peak at −2 ppm). This may suggest that a very fine scale phase separation is taking place at lower fictive temperatures, with a boron-rich phase forming. This is not obvious to the naked eye and the most obvious change is in the NABS-3 specimen with T_f = strain pt. While this thermal history is of the least practical interest since it requires arduous thermal treatment, it may also have some impact on the indentation deformation behavior and the transition to normal cracking. The hypothesis of fine scale phase separation at lower fictive temperatures is further supported by the unexpected, but minor increases in the fraction of N_4 as the fictive temperature is increased. This also supports the hypothesis that boron is segregating a lower fictive temperature. Transmission electron microscopy will be conducted in future work to confirm or refute this explanation.

The subset of glasses that form the boundary forming annular crack offers a unique solution to maximize damage resistance. The annular crack provides a boundary that blocks the extension of radial cracks, even following thermal shock events, as shown in Fig. 8. This material, commercialized as Corning® Fusion5®, found an initial application as a crack-resistant automotive windshield glass. Since Vickers' contact so closely replicates the rock strikes that cause windshield breakage, this solution was found to be ideal.[16,17]

Conclusions

The characterization of glasses as normal or anomalous regarding indentation response is adequate for extreme endpoint glasses such as soda-lime and silica. Most current technical silicate glasses fall somewhere between these two endpoints, with less shear than soda-lime and less densification than silica. By considering the indentation response as a continuum, we can target and explore unique combinations of deformation modes. Previously, so-called intermediate glasses were examined that were directly between soda-lime and silica in the proportions of shear and densification. In the intermediate space, highly crack resistant glasses were discovered that dissipated the indentation energy through highly delocalized, fault-free shearing. Another mechanically advantageous space is identified in this current study near the anomalous end of the deformation continuum, but having more volume-conserving shear than fully anomalous glasses like silica. The anomalous densification contribution ensures a driving force for typical cone cracking, while the shearing contribution provides the residual stress that drives the cone crack back to the surface to create the boundary forming annular crack. The name "boundary forming annular crack" was coined since it prevents radial crack extension, even during extreme thermal shock events. Combining the modes of deformation in various proportions through careful glass design enables us to tailor indentation responses and invent new and highly damage resistant materials. The plot shared here for the deformation continuum highlights some of the novel indentation responses found thus far, but open space remains that is ripe for exploration.

Author contributions

Fulmer, Brian D: investigation (equal) and writing – review & editing (equal). Gross, Timothy M: formal analysis (equal); investigation (lead); and writing – original draft (lead). Jones, Josh (S&T): formal analysis (equal); investigation (equal); and writing – review & editing (equal). Price, James J Dr: investigation (equal). Singh, Keshaan: formal analysis (equal); investigation (equal); and writing – review & editing (equal). Wu, Jingshi: formal analysis (equal); investigation (equal); and writing – review & editing (equal). Yongsunthon, Ruchirej: formal analysis (equal); investigation (equal); and writing – review & editing (equal). Youngman, Randall E: formal analysis (equal); investigation (equal); and writing – review & editing (equal).

Conflicts of interest

There are no conflicts to declare.

Data availability

Additional data cannot be made available due to confidentiality requirements.

References

1 J. E. Neely and J. D. Mackenzie, *J. Mater. Sci.*, 1968, **3**, 603, DOI: 10.1007/BF00757906.
2 K. W. Peter, *J. Non-Cryst. Solids*, 1970, **5**, 103, DOI: 10.1016/0022-3093(70)90188-2.
3 F. N. Ernsberger, *J. Non-Cryst. Solids*, 1977, **25**, 293.
4 J. T. Hagan and M. V. Swain, *J. Phys. D: Appl. Phys.*, 1978, **11**, 2091.
5 A. Arora, D. B. Marshall, B. R. Lawn and M. V. Swain, *J. Non-Cryst. Solids*, 1979, **31**, 415.
6 J. T. Hagan, *J. Mater. Sci.*, 1979, **14**, 462.
7 J. T. Hagan, *J. Mater. Sci.*, 1980, **15**, 1417.
8 R. F. Cook and G. M. Pharr, *J. Am. Ceram. Soc.*, 1990, **73**, 787, DOI: 10.1111/j.1151-2916.1990.tb05119.x.
9 T. M. Gross, J. Wu, D. E. Baker, J. J. Price and R. Yongsunthon, *J. Non-Cryst. Solids*, 2018, **494**, 13, DOI: 10.1016/j.jnoncrysol.2018.04.048.
10 S. Yoshida, J.-C. Sangleboeuf and T. Rouxel, *J. Mater. Res.*, 2005, **20**, 3404.
11 J. D. Mackenzie, *J. Am. Ceram. Soc.*, 1963, **46**, 461.
12 E. H. Yoffe, *Philos. Mag. A*, 1982, **16**, 617.
13 T. M. Gross, *J. Non-Cryst. Solids*, 2012, **358**, 3445.
14 S. Bista, J. F. Stebbins, J. Wu and T. M. Gross, *J. Non-Cryst. Solids*, 2017, **478**, 50.

15 J. Wu, T. M. Gross, L. Huang, S. P. Jaccani, R. E. Youngman, S. J. Rzoska, M. Bockowski, S. Bista, J. F. Stebbins and M. M. Smedskjaer, *J. Non-Cryst. Solids*, 2020, **530**, 119797.
16 T. M. Cleary, T. M. Gross and J. Wu, *US Pat.*, 11,951,713, 2024.
17 T. M. Cleary, T. M. Gross and J. Wu, *US Pat.*, 12,122,714, 2024.
18 ASTM International, ASTM C693-93, 2019.
19 ASTM International, ASTM E228-22, 2023.
20 ASTM International, ASTM C1350-96, 2019.
21 ASTM International, ASTM C1351M-96, 2022.
22 ASTM International, ASTM C623-21, 2021.
23 ASTM International, ASTM C1648-12, 2018.
24 T. M. Gross and R. Youngman, in *Flexible Glass: Enabling Thin, Lightweight, and Flexible Electronics*, ed S. Garner, Wiley, New York, 2017, pp. 63–83.
25 D. Massiot, F. Fayon, M. Capron, I. King, S. Le Calve, B. Alonso, J. O. Durand, B. Bujoli, Z. Gan and G. Hoatson, *Magn. Reason. Chem.*, 2002, **40**, 70.
26 D. R. Neuville, L. Cormier and D. Massiot, *Geochim. Cosmochim. Acta*, 2004, **68**, 5071.
27 L.-S. Du and J. F. Stebbins, *J. Non-Cryst. Solids*, 2003, **315**, 239.
28 H. Aben and C. Guillement, *Photoelasticity of glass*, Springer-Verlag, Berlin (1993).
29 H. Yamashita, H. Yashino, K. Nagata, H. Inoue, T. Nakajin and T. Maskawa, *J. Non-Cryst. Solids*, 2000, **270**, 48, DOI: 10.1016/S0022-3093(00)00056-9.
30 L.-S. Du and J. F. Stebbins, *J. Phys. Chem. B*, 2003, **107**, 10063.
31 Z. N. An, W. D. Li, F. X. Liu, P. L. Liaw and Y. F. Gao, *Metall. Mater. Trans. A*, 2012, **43**, 2729, DOI: 10.1007/s11661-011-0992-5.
32 T. M. Gross, in The World Scientific Reference of Amorphous Materials: Structure, Properties, Modeling, and Main Applications, *Vol 2. -Structure, Properties, and Applications of Oxide Glasses*, ed P. C. Taylor and I. E. Reimanis, World Scientific, New Jersey, 2021, pp. 99–164.
33 R. Tandon, D. J. Green and R. F. Cook, *J. Am. Ceram. Soc.*, 1990, **73**, 2619.